Extended slow-light field enhancement in positive-index/negative-index heterostructures

S. Foteinopoulou[1,*] and J. P. Vigneron[2,†]
[1]*School of Physics, CEMPS, University of Exeter, Stocker Road, Exeter EX4 4QL, United Kingdom*
[2]*Facultes Universitaires Notre-dame de la Paix (FUNDP), Namur, Belgium*
(Received 17 May 2013; revised manuscript received 7 November 2013; published 22 November 2013)

We present a biwaveguide paradigm composed of joined positive-index-material (PIM)/negative-index-material (NIM) slabs, demonstrating ultraslow-light propagation stemming from the competing propagation disposition in the PIM and NIM regions. We report for the first time a mesoscopic extended electromagnetic (EM) enhancement covering regions of the order of the free-space wavelength, enabled by the slow-light mode in our system. Our dynamic numerical results are consistent with our developed theoretical model, predicting an EM energy accumulation reminiscent of a charging capacitor. Our analysis reveals that spatial compression is not a requirement for EM enhancement in slow-light systems and stresses the merits of a high coupling efficiency, strong temporal compression, monomodality, and modal index bandwidth—all present in our proposed paradigm. Furthermore, we show that the heterostructure waveguide mode is an extraordinary entity with a unique energy velocity, which is opposite to the Poynting vector in one of the participant waveguides. We believe that these results will inspire new slow-light platforms relevant to the collective harvesting of strong light-matter interactions.

DOI: 10.1103/PhysRevB.88.195144 PACS number(s): 42.25.−p, 42.82.Et, 78.67.Pt, 81.05.Xj

I. INTRODUCTION

Slow light has attracted increasing attention in recent years owing to its tremendous application potential, as, for example, in all-optical chips[1–3] and optical memories.[2] Slow light has furthered the frontiers of current optics, with many works reporting on strong light-matter interactions that manifest themselves as an enhancement of optical gain,[1,4] Raman signal[5] or nonlinear optical processes,[1,4] such as third-harmonic generation.[6] Strong light-matter interactions are associated with high-intensity electromagnetic (EM) fields. Intensity enhancing platforms have been pursued vigorously in recent years; they involve a spatial compression of the impinging wave into deep-subwavelength volumes. Typically, spatial light compression is facilitated by a resonant[7–10] interaction between light and a structured material, although a nonresonant[11] scheme has also been demonstrated recently.

Slow-light physics is opening an alternate avenue where field enhancement may occur as a result of temporal compression,[1,2] thus allowing it, in principle, to extend over mesoscale areas of the order of the free-space wavelength. This can facilitate a collective harvesting of light-matter interaction, which is important when a strong signal yield from nonlinear optical processes is desired. With the exception of resonant atomic systems,[12] all slow-light paradigms[2] seem promising in terms of field enhancement, which has been indirectly evidenced by observing a dependent process.[5,6,13] However, a deeper understanding is still lacking with respect to which are the key controlling attributes pertinent to the dynamics of EM energy enhancement in slow-light platforms. Also, there seems to be a lack of a clear consensus regarding the role of spatial compression in slow-light systems.[2,4]

Different schemes have been employed to control the light's dispersion and thus the speed of information transfer in man-made architectures.[1,2,4,13–21] An interesting scheme was proposed in 2006 by Vandenbem *et al.*[22] that joins a positive-refractive-index medium (PIM) with a negative-refractive-index medium (NIM)[23] together into a heterostructure waveguide,[24] shown to exhibit a flat photonic dispersion.[22] Other NIM-based waveguides were also reported by Shadrivov *et al.*[25] and Tsakmakidis *et al.*,[26] but with the energy being guided through the NIM only, evanescently decaying outside. In the system of Ref. 26 a slow-light behavior leading to rainbow trapping via an adiabatic taper was predicted by frequency-domain calculations. Given the ongoing rapid development of photonic metamaterials,[27,28] these NIM-based waveguides seem highly promising as slow-light platforms. However, the salient dispersion features relevant to an achievable ultrahigh slowdown factor, as well as the related unconventional propagation characteristics within a wave-optics picture, have not been identified. Furthermore, the peculiar dynamics of energy accumulation in these systems, and its relation to spatial and temporal compression, is certainly still outstanding. It should also be noted that efficient coupling to slow-light modes is not a trivial matter and is the subject matter of currently ongoing research.[29,30]

In this paper, we propose a particular PIM-NIM heterostructure as a composite biwaveguide paradigm and discuss its extraordinary dispersion features in Sec. II. In Sec. III we present time-domain simulations that verify the existence of the trapped slow mode—predicted by the frequency-domain simulations in Sec. II—and also demonstrate an associated high EM enhancement covering mesoscale areas, of the order of the wavelength. In Sec. IV we further analyze the propagation characteristics of the slow mode and report for the first time an exotic guided wave having a Poynting vector that is opposite to the direction of energy propagation in one of the participant waveguides. These dynamic observations further stress the importance of the large modal-index bandwidth that we discuss in Sec. V. Furthermore, in Sec. VI we study the EM energy accumulation for the slow mode in the time domain. We present an analytical model that underpins the observed dynamic EM energy accumulation, which reveals the participating roles of spatial and temporal compression. This model identifies the prominent features of our prototype's band dispersion that are responsible for

both observing ultraslow light and achieving an extended high field enhancement. Finally, we present our conclusions in Sec. VII.

II. THE NIM-PIM BIWAVEGUIDE PARADIGM

In Fig. 1(a) we show a schematic of the biwaveguide paradigm, with its geometric characteristics designated (we assume an infinite extent in the x and z directions). We take a dielectric medium for the PIM ($\varepsilon_2 = 4.0$, $\mu_2 = 1.0$) and consider a homogeneous left-handed medium[23] for the NIM, similar to the one in Refs. 31–33. In particular, we take

$$\varepsilon_1 = \mu_1 = 1 - \frac{\omega_p^2}{\omega^2}, \tag{1}$$

with $\omega_p = 2\pi \times 308 \times 10^{12}$ rad/s and ω representing the frequency of the EM wave. We investigate the H-polarized composite guided modes; i.e., light is guided within both the NIM and the PIM layers of the biwaveguide and has evanescent tails outside, with the magnetic field along the z direction. Our design prototype has $d_1 = 1702.5$ nm and $d_2 = 2837.5$ nm.

By assuming guided waves in both the NIM and the PIM regions and evanescent tails outside (see also the Appendix), we obtain the dispersion relation for the composite NIM-PIM biwaveguide guided mode, $\omega(k_{||})$, where $k_{||}$ is the wave vector along the x axis. This is given by

$$\frac{(z_1 + z_2)\cos OP + (1 - z_1 z_2)\sin OP}{(z_1 - z_2)\cos \Delta OP + (1 + z_1 z_2)\sin \Delta OP} = \frac{z_1 - z_2}{z_1 + z_2}, \tag{2}$$

where $OP = k_{1y} d_1 + k_{2y} d_2$, $\Delta OP = k_{1y} d_1 - k_{2y} d_2$, $z_1 = \frac{k_{1y}}{\varepsilon_1 k_y}$, and $z_2 = \frac{k_{2y}}{\varepsilon_2 k_y}$. k_y represents the decaying wave vector outside the biwaveguide, while k_{1y} and k_{2y} represent the wave vectors along the y axis inside the negative-index part and positive-index part of the biwaveguide, respectively. That is,

$$k_y = \sqrt{k_{||}^2 - \frac{\omega^2}{c^2}}, \tag{3}$$

$$k_{1y} = \sqrt{\varepsilon_1 \mu_1 \frac{\omega^2}{c^2} - k_{||}^2}, \tag{4}$$

and

$$k_{2y} = \sqrt{\varepsilon_2 \mu_2 \frac{\omega^2}{c^2} - k_{||}^2}, \tag{5}$$

with c being the speed of light.

We solve Eq. (2) as a transcendental equation and show the result for the photonic dispersion by the solid line in Fig. 1(b). Note the biwaveguide mode transitions from a region of a positive band slope to a region of a negative band slope with increasing $k_{||}$. Essentially, this implies that the guided mode transitions from being forward to being backward[34] upon passing through a regime with near-zero $d\omega/dk_{||} = v_g$, implying near-frozen light [see also the dashed line in Fig. 1(c)]. Now, this by itself may not be striking and occurs also in systems where the EM energy is guided through the left-handed-medium core only.[25] However, what is striking is that the near-zero v_g regime extends over a much larger $k_{||}$ interval, which we henceforth refer to as the modal-index bandwidth.[35] This extraordinary feature has been observed in photonic-crystal waveguides[2,17] but, in these systems, does not

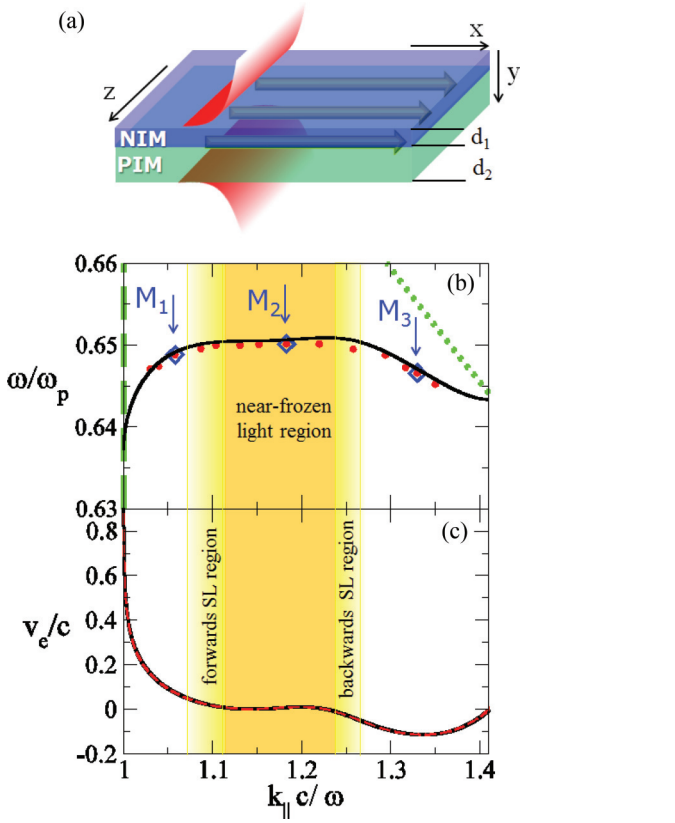

FIG. 1. (Color online) (a) Schematic of the PIM-NIM biwaveguide. (b) Photonic dispersion (theory) of the biwaveguide's guide mode (solid black line), with the dashed (dotted) line representing the light line in vacuum (in the NIM). (Not shown here is the light line in the PIM at much larger $k_{||}$.) Filled circles represent the corresponding numerical time-domain result, with open diamonds designating three characteristic cases, labeled M_1, M_2, and M_3. Both the frequency, ω, and the x component of the wave vector, $k_{||}$, are scaled to be dimensionless (ω_p defines the material properties of the NIM). The dark shaded area shows the near-frozen light regime, which merges to a regime with slow backward (slow forward) light to the right (the left) (lighter shaded area). (c) The corresponding energy velocity (solid line) and group velocity (dashed line), both scaled by the speed of light c.

routinely come with monomodality. Cross-modal talk directs EM energy away from the slow-light channel, thus being a major hurdle in the performance of photonic-crystal-based platforms. On the other hand, monomodality is an inherent advantage in these metamaterial biwaveguides[24] and flat bands with a large modal-index bandwidth can be easily tailored with proper choice of d_1 and d_2.[22] We note that the key importance of these essential characteristics has not been discussed for other NIM-based slow-light platforms,[26] where the light slowdown factor has not been observed in the time domain.[31]

We highlight in Fig. 1 the modal-index bandwidth for near-frozen light by the dark shaded region, which transitions to the left and the right to a $k_{||}$ region of forward and backward faster light, respectively. Note that the composite guide mode is on the right side of the air light line (dashed line) but on the left side of the light lines in the NIM (dotted line) and in the PIM (not shown since it is much farther to the right than the figure

bounds). This signifies the guided-wave nature of the mode within both the PIM and the NIM parts of the biwaveguide heterostructure. We also stress that indeed the group velocity of our system [dashed line in Fig. 1(c)] portrays the velocity of energy propagation, v_e[23] [solid line in Fig. 1(c)] (see the Appendix).

III. DYNAMIC BEHAVIOR OF LIGHT IN THE NIM-PIM BIWAVEGUIDE

In the following, we study the dynamic behavior of light in our proposed paradigm. For this purpose we employ the finite-difference time-domain (FDTD) method,[36,37] a proven excellent method for capturing the time evolution of EM waves while propagating in space even within NIMs.[33,38] To excite the composite guided mode in the biwaveguide heterostructure we employ in the FDTD an attenuated total reflection (ATR) setup[40,42] in the Otto configuration[39] as depicted in Fig. 2(a).[40] The refractive index of the prism, n_{atr}, varies as required to yield the desired $k_{||}$ value.[41] In this manner, we can select from the entire band in Fig. 1(b) a specific band region centered around modal index $ck_{||}/\omega$,[35] with a bandwidth that is inversely proportional to the beam waist of the incident Gaussian beam, depicted in the schematic in Fig. 2(a) with its magnetic field polarized out of the prism plane.

We have confirmed the band dispersion numerically, by considering a pulsed impinging signal and recording the Fourier-transformed spectral response of properly placed detectors above the prism and laterally within the biwaveguide. We show our results as filled circles in Fig. 1. We highlight there three particular modes that we represent by open diamonds and name M1, M2, and M3. These have, respectively, a positive, a near-zero, and a negative band slope, implying forward, slow-light, and backward propagation in each case.

With a quasimonochromatic excitation[43] at the relevant frequency in FDTD we confirm the forward and backward lateral propagation as shown in Figs. 2(b) and 2(d), respectively, where the time-averaged electric-field intensity is shown cropped around the waveguide area. [See also Figs. 3(a) and 3(c), respectively, where the ATR prism excitation area is included.] Now, mode M2, shown in Fig. 2(c) [or Fig. 3(b)], is mostly forward propagating, but we see some EM energy escaping to the opposite side, due to the unavoidable nonzero $k_{||}$ bandwidth of the impinging Gaussian source. What is striking is the much higher intensity enhancement with respect to the intensity of the input beam that is associated with this mode.

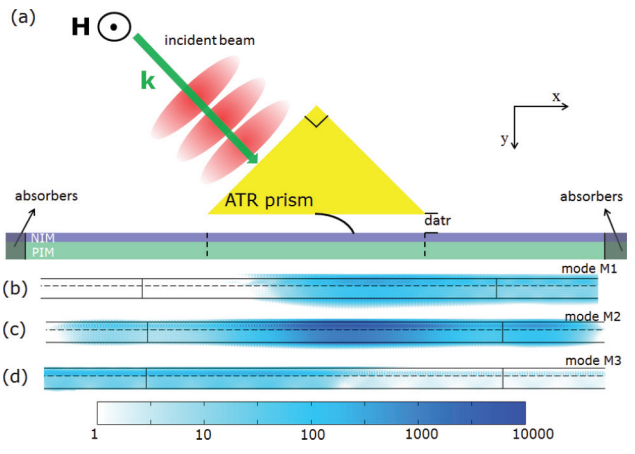

FIG. 2. (Color online) (a) Schematic of the numerical FDTD ATR experimental setup. (b–d) FDTD result for the time-averaged electric field intensity, I, for mode M1 (b), mode M2 (c), and mode M3 (d). The domain is cropped to depict I only in the vicinity of the biwaveguide, -extending within the solid horizontal lines in the figure. Vertical lines delimit the biwaveguide region that lies directly below the ATR prism, while dotted lines designate the NIM-PIM boundary. The color map scale is logarithmic.

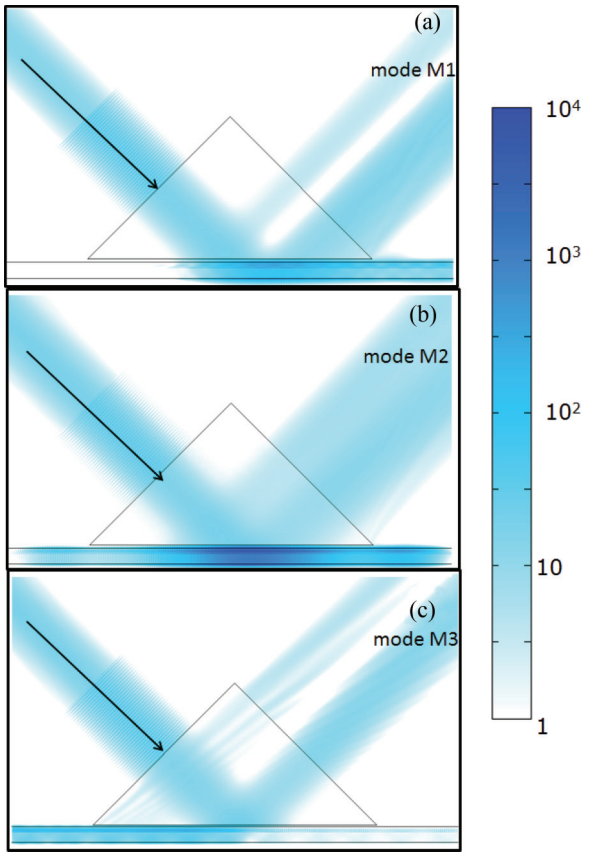

FIG. 3. (Color online) Same as Figs. 2(b)–2(d), but with the ATR excitation region included. The triangle represents the ATR prism, used to excite the guided modes, while the solid horizontal lines represent the biwaveguide limits.

IV. INTERLOCKING OF THE NIM AND PIM SUBMODES WITH COUNTER-DIRECTIONAL POYNTING VECTORS

We proceed by analyzing further the curious characteristics of the composite slow-light mode in the heterostructure biwaveguide. For this purpose, we launch in the FDTD simulation a narrow-bandwidth pulsed signal[44] and observe the Poynting vector within each of the joint waveguides. We monitor the x component of the Poynting vector at different lateral locations, at the right side of the prism for the forward modes, i.e., modes M1 and M2, and at the left side of the prism for the backward mode, i.e., mode M3. Let D_{det} represent the distance between the lateral line detectors and the relevant

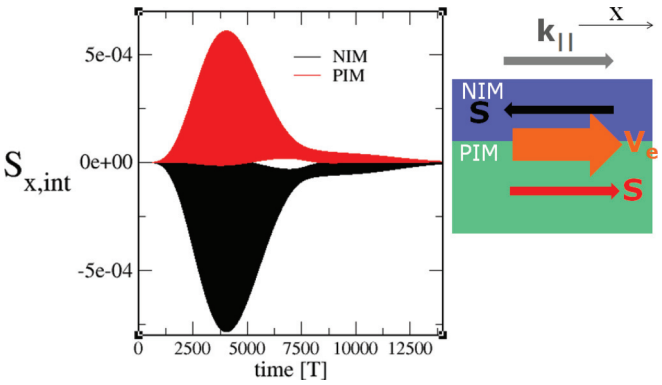

FIG. 4. (Color online) Interlocking of the submodes within each layer of the heterostructure waveguide, observed in the FDTD for mode M2 via the x component of the Poynting vector monitored at the right of the ATR prism edge. The black line and the lighter (red) line represent the results integrated over the y extent of the NIM part and PIM part of the biwaveguide, respectively. The Poynting vector is given in arbitrary units, while time is expressed in terms of the period T of the central frequency ω_0 of the pulsed signal. Clearly, the submodes move together towards the $+x$ direction, despite the Poynting vector pointing towards the $-x$ direction in the NIM layer. The schematic on the right indicates the wave vector $\mathbf{k}_{||}$ and energy velocity $\mathbf{v_e}$ of the composite guided mode, as well as the Poynting vector $\mathbf{S}$ in each of the subwaveguides.

side of the prism edge. For each lateral location, D_{det}, one line detector is placed within the NIM part of the biwaveguide and one line detector is placed within the PIM of the biwaveguide. Then, for each time step, the x component of the Poynting vector S_x is integrated along the respective line detectors in the NIM and PIM parts of the biwaveguide. We represent this integrated value as $S_{x,\text{int}}$. In Fig. 4 we show the result for mode M2 and $D_{\text{det}} = 2.27\ \mu$m. We show the respective results for modes M1 and M3 in Fig. 5.

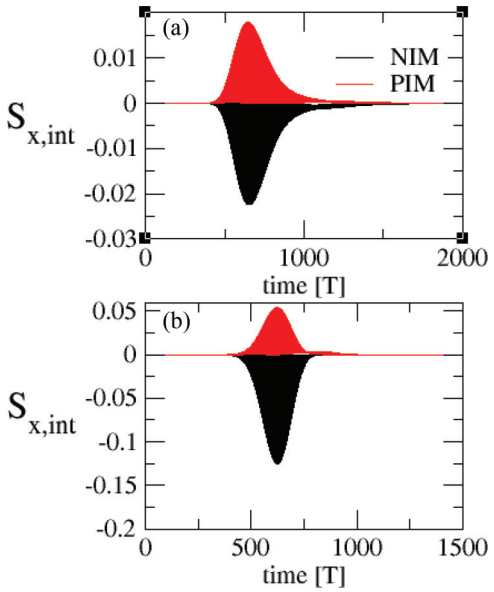

FIG. 5. (Color online) Same as Fig. 4, but for the cases of (a) mode M1 and (b) mode M3.

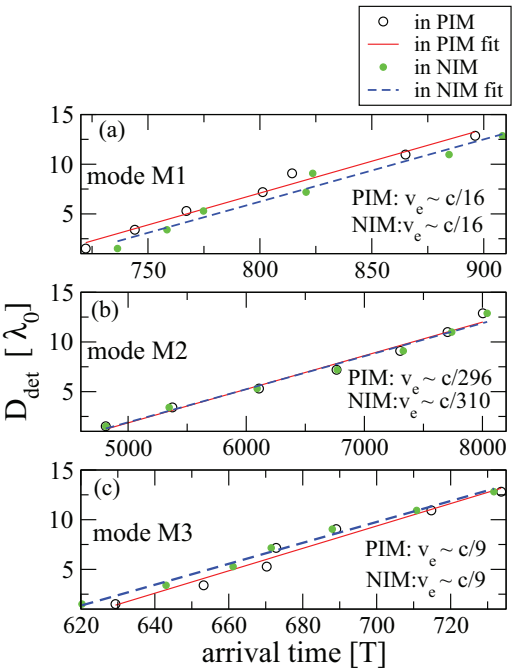

FIG. 6. (Color online) Pulse arrival times in the NIM (PIM) part of the biwaveguide in the different lateral detectors represented by filled (open) circles. The arrival time is given in terms of the period; the lateral detector locations D_{det}, in terms of the wavelength that corresponds to the central frequency ω_0 of the impinging pulse. The line fit in each case yields the energy velocity of propagation in each subwaveguide.

We find that the pulse propagates laterally, i.e., along the x-direction, consistent with a wave-optics picture. A geometric optics picture, previously employed to explain slow-light propagation in Ref. 26, clearly fails, as it implies a significant Poynting vector component along the y direction, which we did not observe in our simulations. We observe in the FDTD a truly astonishing phenomenon: the Poynting vector is antiparallel to the direction of EM energy propagation in one of the participant waveguides. Specifically, the Poynting vector consistently points towards the $-x$ direction in the NIM layer and towards the $+x$ direction in the PIM layer in all cases. Indeed, in all cases the submodes within each of the participant waveguides interlock together. They move jointly, as an entity, towards the same direction that is determined by the band slope of the dispersion relation, $\omega(k_{||})$, despite the counter-directional relation of the Poynting vector within each layer of the heterostructure waveguide.

The behavior of the guided waves within each subguide as an entity can be further evidenced by observing in the FDTD simulation the arrival time[45] of the pulsed signal at different locations at the right side of the prism (for modes M1 and M2, which are forward) or the left side of the prism (for mode M3, which is backward) (Fig. 6). The pulse arrival time within the NIM and PIM parts of the biwaveguide, at the different lateral locations, is calculated from the detected $S_{x,\text{int}}$ with time. Normally, in experiments or simulations the arrival time of a pulse is determined by the peak of the pulse. However, this is a rough method and can entail significant errors for systems in which significant pulse broadening occurs during

propagation. This is particularly true for slow-light systems. Petross *et al.*[45] have proposed an accurate measure for the pulse arrival time for nonstandard systems, which we employ here. Thus, we calculate the pulse arrival time, $t_{\rm arr}$, at a certain lateral line detector, $D_{\rm det}$, from the relation

$$t_{\rm arr} = \frac{\int_0^{t_{\rm sim}} t\, S_{x,\rm int}(D_{\rm det},t)dt}{\int_0^{t_{\rm sim}} S_{x,\rm int}(D_{\rm det},t)dt}, \qquad (6)$$

with t being the instant in time at which $S_{x,\rm int}$ is monitored at the line detectors in the NIM and PIM parts of the biwaveguide at the $D_{\rm det}$ lateral location. Also, $t_{\rm sim}$ is the total simulation time. Note, since we have different line detectors placed in the participant waveguides of the heterostucture, the arrival time is recorded separately in the NIM and PIM parts of the biwaveguide.

We plot the results for the arrival time at the different lateral detector positions, $D_{\rm det}$, in Figs. 6(a), 6(b), and 6(c) for modes M1, M2, and M3, respectively. The filled circles represent the arrival times calculated in the NIM part of the biwaveguide. Conversely, the open circles represent the arrival times calculated in the PIM part of the biwaveguide. The excellent agreement between the two supports further our previous observation that the composite mode is an entity, and EM energy propagates at the same speed within the entire extent of the waveguide, within both the NIM and the PIM parts.

Now we can take a linear fit in each case, and from this we obtain the energy velocity of the composite mode. We express this in terms of the speed of light c in each case and show it in the respective figures. Indeed, the observations for the energy velocity within the NIM and PIM parts of the biwaveguide are in excellent agreement, further attesting that the EM energy of the composite mode propagates at a unique speed in all parts. We have expressed the results in fractional form, so the slowdown factor is immediately evident. We find a slowdown factor of ∼16 for mode M1, ∼303 for mode M2, and ∼9 for mode M3.

To compare with the theoretical predictions from the dispersion relation we use the slowdown factors from Fig. 1, which correspond to the central $k_{||}$ of the impinging Gaussian beam; these are ∼13 for mode M1, ∼105 for mode M2, and ∼9 for mode M3. We observe an excellent agreement for modes M1 and M3 but we find that mode M2 is slower than expected. This is because the finite spatial extent of the impinging beam implies a $k_{||}$ span within a band $\Delta k_{||}$. Thus in practical situations one observes the average speed from the mode contributions within this $\Delta k_{||}$ band. For mode M2, this ended up yielding a slowdown factor even higher than the one predicted for the central $k_{||}$ value.

V. SLOW-LIGHT PROPAGATION AND MODAL-INDEX BANDWIDTH

Our analysis in Sec. IV suggests that the overall speed of EM energy propagation is affected by the finite spatial extent of the impinging Gaussian beam, implying contributions from within a $\Delta k_{||}$ band. This further highlights the particular advantage of having a wide modal-index span over which the composite biwaveguide mode is near-frozen, as shown in

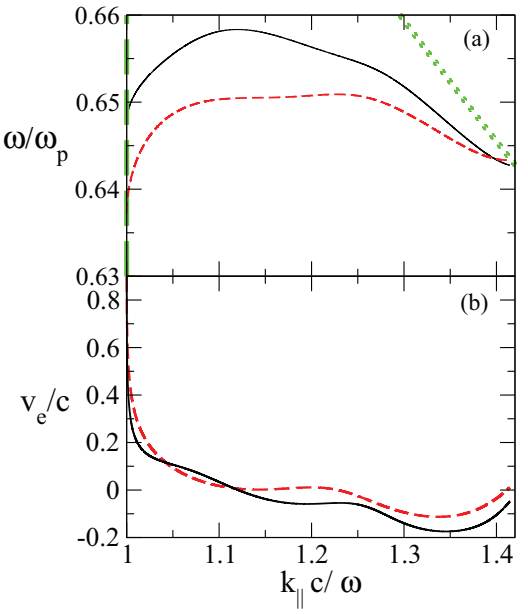

FIG. 7. (Color online) (a) Photonic band dispersion and (b) energy velocity are shown by the solid black lines for a comparative biwaveguide design with $d_1 = 2270$ nm and $d_2 = 3405$ nm. The long-dashed and dotted (green) lines represent the relevant light lines as in Fig. 1. To aid comparison, we show the respective result for the original design in Fig. 1 with dashed (red) lines.

Fig. 1. For example, let us consider a comparative design with $d_1 = 2270$ nm and $d_2 = 3405$ nm. We show the dispersion relation $\omega(k_{||})$ and corresponding energy velocity (in units of speed of light c) for the latter design in Figs. 7(a) and 7(b), respectively. In order to be able to easily compare the result with the system in Fig. 1, we also show the respective dispersion and energy velocity, as dashed lines. Evidently the band for the comparative design is not as flat. A near-frozen mode exists only for a very narrow $k_{||}$ band.

We further investigate in the FDTD the implications of the lack of existence of a wide modal-index bandwidth. We set the ATR prism properties to excite in the comparative design the near-frozen mode of $ck_{||}/\omega = 1.12$, as predicted from the photonic dispersion in Fig. 7. Yet what we observe (see Fig. 8) is an amphoteric propagation. This emanates from the strong

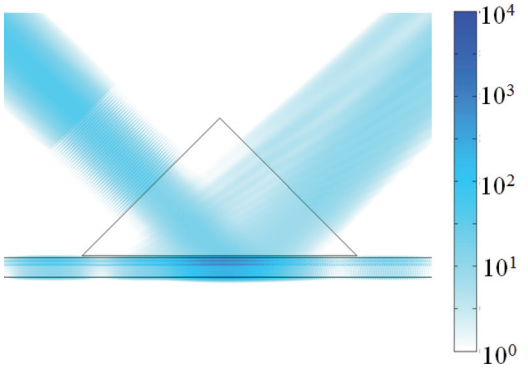

FIG. 8. (Color online) FDTD time-averaged intensity result, suggesting an amphoteric propagation in the comparative waveguide design of Fig. 7 for the near-frozen mode of $ck_{||}/\omega = 1.12$.

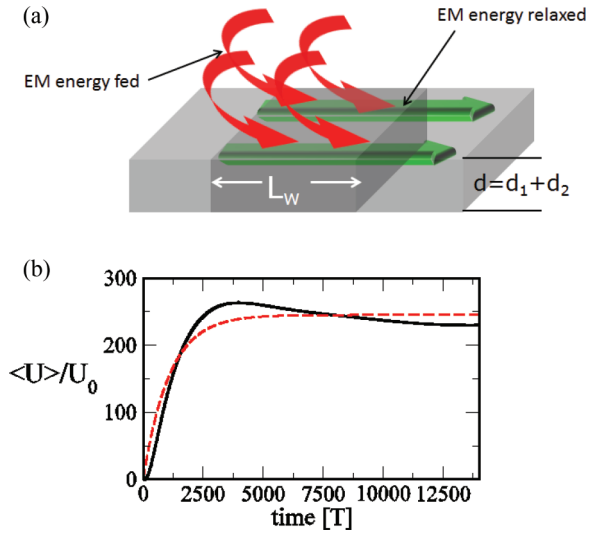

FIG. 9. (Color online) Energy accumulation dynamics in the biwaveguide paradigm. (a) The feeding of EM energy from above via the ATR prism and its relaxation sideways in the biwaveguide. (b) The solid black line represents the FDTD result for the time-averaged EM energy density of the spatial average in the biwaveguide region below the center of the ATR prism $\langle U \rangle$ for mode M2, normalized by the time-averaged energy density of the source U_0. The dashed (red) line represents the fit from an analytical dynamical model in accordance with the plot in (a).

contributions from the adjacent backward and forward modes, as the near-frozen mode has a narrow modal-index bandwidth in the comparative waveguide. The latter cannot be avoided due to the finite spatial extent of any realistic excitation beam. These results suggest that the near-frozen light modal-index bandwidth is the key feature of merit when considering the design characteristics of the biwaveguide.

VI. EM ENERGY ACCUMULATION IN THE BIWAVEGUIDE

Now that we have verified a large slowdown factor for the M2 mode, we try to understand its relation to the observed intensity enhancement shown in Fig. 2(c) [or 3(b)], which spans the entire waveguide width, $d \sim 3\lambda_0$, with λ_0 being the free-space wavelength. Since the waveguide extent in the z direction is infinite, implying that, in practice, the waveguide can be arbitrarily wide in this direction, our results essentially suggest an extended intensity enhancement covering a large mesoscale area, larger than λ_0^2. This, to our knowledge, constitutes the first report of this capability, as typically, intensity enhancement is restricted to deep-subwavelength regions.[7–11]

To understand this further, we excite the M2 slow mode with a quasimonochromatic wave and monitor the time evolution of the EM energy density, spatially averaged over a central region of the biwaveguide lying directly below the ATR prism. We take the time average of this quantity within each wave period T, $\langle U \rangle$, and normalize it with the time-averaged EM energy density of the source U_0. The result in each period T, shown in Fig. 9(b), implies an energy accumulation with an almost-exponential time response reaching a 200-fold EM energy density enhancement at steady state.

Let us consider a simple crude model, depicted in Fig. 9(a), to explain the energy accumulation dynamics. EM energy, $\mathcal{E}$, is fed into the biwaveguide from above via the ATR prism, at a faster rate than its relaxation sideways in the $+x$ direction (M2 is a forward mode),[46] because of the ultralow energy velocity of the M2 mode. In the following we denote by angle braces ($\langle\ \rangle$) the spatially averaged quantities of the energy density, in an area $L_w d$ in the central part of the biwaveguide below the ATR prism, where d represents the total width of the biwaveguide [see schematic in Fig. 9(a)]. By L_w we denote the beam waist of the evanescent wave illumination emanating from the ATR prism, which is close to the Gaussian impinging wave's beam waist. Moreover, time-averaged quantities, within a wave period T are assumed for the EM energy densities U. Note that we have translational symmetry in the z direction, where the guide is assumed to be infinite. We focus on a part of the guide with width $L_{\rm per}$ along z. We see that this chosen part can be arbitrary and does not influence the result. Then, within ΔT, the EM energy that is fed into the waveguide will be

$$\Delta \mathcal{E}_{\rm feed} = F_c I_0 \Delta T L_w L_{\rm per}, \tag{7}$$

where F_c represents the coupling efficiency, and I_0 the intensity of the impinging Gaussian beam. Thus,

$$\Delta \mathcal{E}_{\rm feed} = F_c c U_0 \Delta T L_w L_{\rm per}, \tag{8}$$

where U_0 is the energy density of the impinging beam. Then the energy that gets relaxed sideways within ΔT will be

$$\Delta \mathcal{E}_{\rm rel} = \langle S_x \rangle d L_{\rm per} \Delta T = v_e \langle U \rangle d L_{\rm per} \Delta T. \tag{9}$$

So the increase in EM energy in ΔT will be $\Delta \mathcal{E}_{\rm feed} - \Delta \mathcal{E}_{\rm rel}$. This equals $\langle \Delta U \rangle d L_{\rm w} L_{\rm per}$, yielding, together with Eqs. (8) and (9), that

$$\frac{\Delta \langle U \rangle}{\Delta T} = -\frac{v_e}{L_w}(\langle U \rangle - U_M), \tag{10}$$

where

$$U_m = F_c U_0 \frac{c}{v_e}\frac{L_w}{d}. \tag{11}$$

Equation (10), with Eq. (11), yields

$$\langle U \rangle = U_0 \frac{c}{v_e}\frac{L_w}{d}\left(1 - e^{-\frac{v_e}{L_w}t}\right), \tag{12}$$

where the time should be an integer multiple of period T.

Thus, the estimation of the feeding and relaxation rates leads to a time -response for the EM energy accumulation that is reminiscent of a charging capacitor, with the characteristic time τ being equal to L_w/v_e. Equation (12) implies that spatial compression contributes a factor of L_w/d to the overall EM energy enhancement, which is actually quite modest (about 4) for the biwaveguide paradigm. Temporal compression contributes a large factor for slow-light modes equal to c/v_e. The results in Fig. 9(b) also imply a high coupling efficiency F_c, greater than 60% with our proposed simple ATR-based coupling scheme. We observe that the overall EM energy enhancement factor is not evenly spread within each sub waveguide and is also larger than the corresponding electric-field intensity enhancement (enhancement of EE^*).

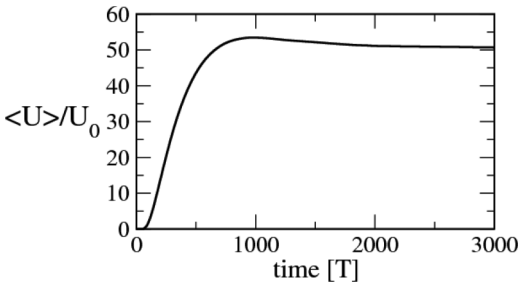

FIG. 10. Same as Fig. 9(b), but for the comparative waveguide of Fig. 7. As a result of the narrow modal bandwidth for the near-frozen mode, a smaller EM energy enhancement and quicker saturation in comparison with the design in Fig. 1 are observed.

Specifically, we find the latter to be about 100 in the NIM layer and about 30 in the PIM layer. Note, also, that the characteristic time of the exponential EM energy growth indirectly provides the light slowdown factor, which we found to be, with an exponential fit, about 90 for the case in Fig. 9(b).[47]

We note that the comparative design yielded a much lower EM energy enhancement, as shown in Fig. 10. This is because additional energy relaxes from the faster backward and forward modes adjacent to the near-frozen mode, as any excitation beam inadvertently includes contributions within a $\Delta k_{||}$ band. Equation (12) simultaneously stresses the need not only for a wide modal-index bandwidth of the near-frozen mode but also for monomodality. Actually, it can be shown that the coexistence of any faster channel significantly hampers the maximum attainable EM energy enhancement.

For example, suppose that light couples inside the composite waveguide with a total coupling efficiency F_c, but to two different modes that coexist with respected weights F_{c1}/F_c and F_{c2}/F_c, with $F_{c1}+F_{c2}=F_c$ and energy velocities v_{e1} and v_{e2}. Then the balance of energy fed and energy released sideways will lead to

$$\langle U\rangle = U_0 \frac{c}{v_e^{\text{eff}}}\frac{L_w}{d}\left(1-e^{-\frac{v_e^{\text{eff}}}{L_w}t}\right), \tag{13}$$

with

$$v_e^{\text{eff}} = \frac{v_{e1}F_{c1}+v_{e2}F_{c2}}{F_c}. \tag{14}$$

Equations (13) and (14) clearly imply that the maximum EM energy enhancement that can be attained is adversely affected by the coexistence of any faster channel. They also indicate that the respective saturation time to the maximum EM energy is smaller. This is consistent with what is shown in Fig. 10 for the energy accumulation for the comparative design in Fig. 7, where part of the impinging light couples to faster channels that are adjacent to the near-frozen mode.

VII. CONCLUSIONS

In conclusion, we have presented a paradigm NIM-PIM heterostructure supporting an exotic composite guide mode having an ultralow-energy velocity across a very broad modal-index bandwidth. We have observed in the FDTD a most extraordinary propagation, where the submodes in each layer of the heterostructure interlock together and move jointly in the same direction, despite the Poynting vector being in the opposite direction in one of the layers. We have verified numerically an efficient coupling to the slow mode, with a speed of about $c/300$, leading to exponential growth in EM energy accumulation, reminiscent of a charging capacitor. Our findings suggest the possibility of achieving an extended electric-field intensity enhancement of the order of 100, facilitated by the near-frozen waveguide mode of ultrawide modal-index bandwidth. We therefore believe that this study will inspire new designs for slow-light platforms for the collective harvesting of strong light-matter interactions.

APPENDIX: ENERGY VELOCITY OF THE COMPOSITE GUIDED MODE

The magnetic-field distribution for the composite guided mode is given by

$$H_z = \begin{cases} \mathrm{A}e^{k_y(y+d_1)}e^{i(k_{||}x-\omega t)} & \text{for} \quad y<-d_1, \\ (\mathrm{B}\sin k_{1y}y+\mathrm{C}\cos k_{1y}y)e^{ik_{||}x}e^{-i\omega t} & \text{for} \quad -d_1\leqslant y\leqslant 0, \\ (\mathrm{D}\sin k_{2y}y+\mathrm{E}\cos k_{2y}y)e^{ik_{||}x}e^{-i\omega t} & \text{for} \quad 0\leqslant y\leqslant d_2, \\ \mathrm{F}e^{-k_y(y-d_2)}e^{ik_{||}x}e^{-i\omega t} & \text{for} \quad y>d_2, \end{cases}$$

where $y=0$ is taken at the PIM-NIM interface. The coefficients in the above H_z field distribution are easily determined from the EM boundary conditions at the three interfaces ($y=-d_1$, $y=0$, and $y=d_2$). Thus both the magnetic-field distribution and the corresponding electric-field distribution can be easily calculated for the composite guided mode. Then its energy velocity, v_e, along the x axis [see schematic in Fig. 1(a)] is given by

$$v_e = \frac{\bar{S}_x}{\bar{U}} = \frac{\frac{1}{8\pi}\int_{-\infty}^{\infty}E_yH_z^*dy}{\frac{1}{16\pi}\int_{-\infty}^{\infty}\left(\frac{\partial(\varepsilon\omega)}{\partial\omega}(E_xE_x^*+E_yE_y^*)+\frac{\partial(\mu\omega)}{\partial\omega}H_zH_z^*\right)dy}, \tag{A1}$$

where the expressions in the numerator and the denominator represent the time-averaged Poynting vector and the time-averaged energy density in CGS units, respectively, integrated along the finite dimension of the composite guide (y axis) and outside to include the contributions from the evanescent tails in vacuum. Hence, the limits span from $-\infty$ to ∞. The general expression for dispersive media[23] is taken for the energy density, with ε being either ε_1 or ε_2 and μ being either μ_1 or μ_2, depending on which region of the biwaveguide y lies within, or $\varepsilon=\mu=1$ for the vacuum region. Evidently, for the nondispersive material regions $\frac{\partial(\varepsilon\omega)}{\partial\omega}=\varepsilon$ and $\frac{\partial(\mu\omega)}{\partial\omega}=\mu$.

*Corresponding author: S.Foteinopoulou@exeter.ac.uk
†Deceased June 24, 2013.

[1] T. F. K. Krauss, J. Phys. D: Appl. Phys. **40**, 2666 (2007).
[2] T. F. K. Krauss, Nat. Photon. **2**, 448 (2008).
[3] M. L. Povinelli, S. G. Johnson, and J. D. Joannopoulos, Opt. Express. **13**, 7145 (2005).
[4] T. Baba, Nat. Photon. **2**, 465 (2008).
[5] S. Sandhu, M. L. Povinelli, and S. Fan, Appl. Phys. Lett. **95**, 081103 (2009).
[6] B. Corcoran, C. Monat, C. Grillet, D. J. Moss, B. J. Eggleton, T. P. White, L. O.'Faolain, and T. F. Krauss, Nat. Photon. **3**, 206 (2009).
[7] F. J. Garcia-Vidal, L. Martin-Moreno, T. W. Ebbesen, and L. Kuipers, Rev. Mod. Phys. **82**, 729 (2010), and references therein.
[8] K. L. Kelly, E. Coronado, L. L. Zhao, and G. C. Schatz, J. Phys. Chem. B **107**, 668 (2003).
[9] S. Foteinopoulou, J. P. Vigneron, and C. Vandenbem, Opt. Express. **15**, 4253 (2007).
[10] J. A. Schuller, E. S. Barnard, W. S. Cai, Y. C. Jun, J. S. White, and M. L. Brongersma, Nat. Mater. **9**, 193 (2010).
[11] G. Subramania, S. Foteinopoulou, and I. Brener, Phys. Rev. Lett. **107**, 163902 (2011).
[12] J. B. Khurgin, Adv. Opt. Phot. **2**, 287 (2010).
[13] M. Soljacic, S. G. Johnson, S. H. Fan, M. Ibanescu, E. Ippen, and J. D. Joannopoulos, J. Opt. Soc. Am. B **19**, 2052 (2002).
[14] N. Papasimakis, V. A. Fedotov, and N. I. Zheludev, Phys. Rev. Lett. **101**, 253903 (2008).
[15] S. Zhang, D. A. Genov, Y. Wang, M. Liu, and X. Zhang, Phys. Rev. Lett. **101**, 047401 (2008).
[16] P. Tassin, L. Zhang, Th. Koschny, E. N. Economou, and C. M. Soukoulis, Phys. Rev. Lett. **102**, 053901 (2009).
[17] H. Gersen, T. J. Karle, R. J. P. Engelen, W. Bogaerts, J. P. Korterik, N. F. van Hulst, T. F. Krauss, and L. Kuipers, Phys. Rev. Lett. **94**, 073903 (2005).
[18] S. A. Schulz, L. O'Faolain, D. M. Beggs, T. P. White, A. Melloni, and T. F. Krauss, J. Opt. **12**, 104004 (2010).
[19] D. Mori and T. Baba, Opt. Express. **13**, 9398 (2005).
[20] E. Di Gennaro, P. V. Parimi, W. T. Lu, and S. Sridhar, J. S. Derov, and B. Turchinetz, Phys. Rev. B **72**, 033110 (2005).
[21] A. Karalis, E. Lidorikis, M. Ibanescu, J. D. Joannopoulos, and M. Soljacic, Phys. Rev. Lett. **95**, 063901 (2005).
[22] C. Vandenbem, S. Foteinopoulou, J. P. Vigneron, and V. Lousse, Paper WD5, presented at Photonic Metamaterials: From Random to Periodic: Topical Meeting and Tabletop Exhibit, Grand Island, Bahamas, June 5–8 (2006).
[23] V. G. Veselago, Sov. Phys. Usp. **10**, 509 (1968).
[24] We note that the same type of biwaveguide made of refractive indices of opposite sign has been studied in the frequency domain for its thickness-tolerant monomodal properties. See A. Alu and N. Engheta, IEEE Trans. Microwave Theory Tech. **52**, 1999 (2004).
[25] I. V. Shadrivov, A. A. Sukhorukov, and Y. S. Kivshar, Phys. Rev. E **67**, 057602 (2003).
[26] K. L. Tsakmakidis, A. D. Boardman, and O. Hess, Nature **450**, 397 (2007).
[27] C. M. Soukoulis and M. Wegener, Nat. Photon. **5**, 523 (2011).
[28] V. M. Shalaev, Nat. Photon. **1**, 846 (2007).
[29] P. Hamel, P. Grinberg, C. Sauvan, P. Lalanne, A. Baron, A. M. Yacomotti, I. Sagnes, F. Raineri, K. Bencheikh, and J. A. Levenson, Opt. Express. **21**, 15144 (2013).
[30] S. Ha, M. Spasenovic, A. A. Sukhorukov, T. P. White, C. M. de Sterke, L. K. Kuipers, T. F. Krauss, and Y. S. Kivshar, J. Opt. Soc. Am. B **28**, 955 (2011).
[31] E. I. Kirby, J. M. Hamm, K. L. Tsakmakidis, and O. Hess, J. Opt. A: Pure Appl. Opt. **11**, 114027 (2009).
[32] J. B. Pendry, Phys. Rev. Lett. **85**, 3966 (2000).
[33] R. Moussa, S. Foteinopoulou, and C. M. Soukoulis, Appl. Phys. Lett. **85**, 1125 (2004).
[34] I. V. Lindell, S. A. Tretyakov, K. I. Nikoskinen, and S. IIvonen, Microwave Opt. Technol. Lett. **31**, 129 (2001).
[35] The modal index of a guided mode is given by $n_M = ck_{||}/\omega$. See, for example, J. C. Knight, Nature **424**, 847 (2003). It is an index characterizing the phase of the guided mode and does not imply any effective material properties.
[36] A. Taflove and S. C. Hagness, *Computational Electrodynamics: The Finite Difference Time-Domain Method* (Artech House, Boston, 2005).
[37] The computational domain is terminated with a perfectly matched absorbing boundary (PML); see J.-P. Berenger, J. Comput. Phys. **114**, 185 (1994).
[38] R. W. Ziolkowski and E. Heyman, Phys. Rev. E **64**, 056625 (2001).
[39] A. Otto, Z. Phys. **216**, 398 (1968).
[40] The setup is similar to the one employed in the following references, for the study of photonic-crystal surface waves: S. Foteinopoulou, M. Kafesaki, E. N. Economou, and C. M. Soukoulis, Phys. Rev. B **75**, 245116 (2007); S. Foteinopoulou, G. Kenanakis, N. Katsarakis, I. Tsiapa, M. Kafesaki, E. N. Economou and C. M. Soukoulis, Appl. Phys. Lett. **91**, 214102 (2007).
[41] $k_{||} = n_{\text{atr}} \frac{\omega}{c} \sin 45^\circ$.
[42] The distance between the prism and the waveguide d_{atr} is adjusted so that the ATR prism is not invasive.[40,42] This can be checked by confirming a small spectral offset between the response recorded by a detector above the prism, capturing the TIR beam, and the response recorded by detectors placed laterally away from the prism edge within the participating waveguides, capturing the guided mode that has coupled in. See also Ref. 40. Lateral absorbers are also placed, to reduce the effects from backreflections from the waveguide edges.
[43] S. Foteinopoulou, E. N. Economou, and C. M. Soukoulis, Phys. Rev. Lett. **90**, 107402 (2003).
[44] The degree of monochromaticity of the impinging pulse, $\Delta\omega/\omega_0$, is less than 1%.
[45] J. Peatross, S. A. Glasgow, and M. Ware, Phys. Rev. Lett. **84**, 2370 (2000).
[46] We neglect here the energy relaxing in the opposite direction due to the $\Delta k_{||}$ span.
[47] The quasimonochromatic excitation has a sharper $\Delta\omega$ span in comparison to the pulsed signal and thus involves a narrower part of the near-frozen light band centered around $ck_{||}/\omega = 1.183$, where theory predicts a slowdown factor of about 100 [see Fig. 1(c)].